Chemical Engineering Science 329 (2026) 123774

Contents lists available at ScienceDirect

Chemical Engineering Science

journal homepage: www.elsevier.com/locate/ces

A lab-scale method for the determination of the particle morphology of reactive metal oxide powders using X-ray scattering techniques

Max Philipp Deutschmann *, Hermann Nirschl

Karlsruhe Institute of Technology, Institute of Mechanical Process Engineering and Mechanics, Straße am Forum 8, Karlsruhe, 76131, Baden-Württemberg, Germany

ARTICLE INFO

Keywords:
Metal fuels
Energy storage materials
Particle characterization
Specific surface area analysis
Small-angle X-ray scattering (SAXS)
Wide-angle X-ray scattering (WAXS)

ABSTRACT

Large-scale energy storage concepts are essential for the transition to renewable energy sources. Metal particles have recently gained significant attention as a viable solution due to their recyclability in large-scale energy storage systems. To ensure the material's long-term durability, a thorough understanding of the interplay between particle properties and process conditions is imperative. This study demonstrates the applicability of lab-scale X-ray scattering techniques (SAXS/WAXS) as a quick and easy-to-apply method to investigate the morphology evolution of iron oxide particles during hydrogen reduction in a solid-gas heterogeneous reaction. The increase in the specific surface area could be quantified at various time points, after the reaction was temporarily interrupted without removing the powder from the reactor. The experimental setup, which involves an optically accessible reactor with reactive oxide particles embedded within a low-Z matrix, also enabled the characterization of iron nucleation and growth of iron nuclei up to 30 nm in size.

1. Introduction

The concept of large-scale energy storage is essential for increasing the fraction of usable energy generated by renewable sources, making new and reliable appoaches in this field crucial for the energy transition. An adequate solution, which is currently the focus of extensive research, involves micron-sized metal particles that release heat during oxidation under defined conditions (Shkolnikov et al., 2011; Julien and Bergthorson, 2017; Bergthorson, 2018; Halter et al., 2023). In a subsequent reduction step, the solid oxide particles can be thermochemically reduced back to metal particles without the emission of CO_2. A lot of research has been made showing the applicability of iron as a suitable metallic and recyclable energy carrier (Dirven et al., 2018; Kuhn et al., 2022; Debiagi et al., 2022; Sohrabi et al., 2024). However, during the recycling step, the process conditions of the reduction step have a strong impact on the particle properties making an adequate recycling of the metal fuel non-trivial. Particle growth and fragmentation or changes in the particle microstructure can have a significant impact on the subsequent oxidation and thus on the usability of the metal particles as an energy storage material. To mention one example, previous work has shown that the initial oxidation rate and the maximum oxidation degree can be incrementally increased with each oxidation–reduction cycle under suitable conditions (Kuhn et al., 2024). This enhancement is most likely attributed to the formation of an inner porosity, which allows for improved mass transfer of the reactants (Li et al., 2017). Hessels et al. (2023, 2022) show how the formation of pores correlate with varying reduction process conditions. They observe that the average pore size increases with temperature. Moreover, their experiments suggest that the hydrogen concentration in the feed gas has hardly impact on the particle morphology.

In general, multiple types of morphological changes have been reported in the literature. Depending on the reducing agent (e.g. CO, H_2) as well as the flow conditions or reaction temperature, the reduced particles can exhibit different microstructures apart from the formation of a porous microstructure: a dense and compact iron structure or fiber-like whisker formations on the particle surface (Gong et al., 2014; Guo et al., 2020; Zhang et al., 2020a). Whisker formation, in contrast to the beneficial formation of a porous microstructure, can lead to efficiency losses. During reduction in a fluidized bed the whiskers have been observed to cause particle agglomeration, which in turn leads to defluidization (Komatina and Heinrich, 2004). In addition to agglomeration effects, particle aggregation must also be considered. Due to the formation of sintering bridges, particularly during reduction in a solid bed, particles may fuse together, reducing their transport properties and handling efficiency. Moreover, particle growth serves as an inhibiting factor for gas transport. According to the literature, particle aggregation becomes problematic above 575°C (Hessels et al., 2023), primarily due to surface diffusion as the underlying mechanism (Matsumura, 1971). The variety of morphological states illustrates the need for optimizing process conditions with regards to particle properties.

* Corresponding author.
E-mail address: max.deutschmann@kit.edu (M.P. Deutschmann).

https://doi.org/10.1016/j.ces.2026.123774
Received 12 January 2026; Received in revised form 5 March 2026; Accepted 11 March 2026
Available online 15 March 2026

In summary, the inner surface area of the solid particles can alter significantly during the reduction of iron oxide and their quantitative change heavily depends on the reaction conditions. However, there is no data available to *quantify* the morphology changes under defined process conditions. Therefore, experiments for a morphology characterization, including the specific surface area quantification of the reacting particles, are required. This quantification, combined with the detection of iron nucleation, can be achieved using small-angle X-ray scattering (SAXS).

Based on the proposed method of Spalla et al. (2003), several researchers evaluate the specific surface area of a powder sample with known elemental composition via SAXS by normalizing the intensities on the solid sample thickness of the powder (Schlumberger et al., 2022; Chavez Panduro et al., 2012; Bouzakher-Ghomrasni et al., 2021), e.g., Bouzakher-Ghomrasni et al. (2021) apply this method of the specific surface area determination for several TiO_2 nanoparticle powder samples and they distinguish the location of the Porod regimes between the samples. In the literature, the surface-to-volume ratio evaluation for the analysis of particles in suspensions is also described, e.g., for analyzing bio-molecules like proteins or enzymes and their morphological state within the suspension (Rambo and Tainer, 2011). However, for gas-solid reactions with high-Z materials like metals the analysis of pure powders is hard to apply due to their high X-ray absorption. For this purpose, it is recommended to specifically analyze the specific surface area of the reactive component within a multicomponent system, consisting of a mixture of the reactant and another powder (low-Z material). To the author's knowledge, there is a lack of studies in the literature addressing the specific surface area analysis of reacting metal particles. For this reason, a lab-scale method is proposed to analyze the particle morphology changes within a reacting powder at various time points without removing the particles from the reaction setup.

2. Theoretical background

2.1. X-ray scattering techniques

Small- and Wide-Angle X-ray Scattering (SAXS/ WAXS) are destruction-free scattering techniques for particle analysis. While SAXS can provide information about particle size and morphology, WAXS provides insights into the chemical composition. For crystalline samples, the wide-angle scattering data corresponds to that obtained from X-ray diffraction (XRD) experiments.

Both techniques can be applied in the same setup, allowing particle properties and composition to be determined either simultaneously or sequentially in a one-detector setup. With appropriate temporal resolution, for example, through a sufficiently high intensity of the primary beam, the state of solid-state reactions can be tracked in situ and operando. In this work, the measurements are conducted after temporarily interrupting the reaction, but they are not time-resolved, as laboratory-scale X-ray scattering setups often cannot provide sufficiently high beam intensities. However, the particle characterization is performed while the particles remain within the reactor, thereby avoiding morphological changes due to particle handling. The SAXS analysis will focus on the determination of the specific surface area of loose powders based on the method provided by Spalla et al. (2003).

2.2. Small-angle scattering

Small-angle X-ray scattering is founded on the elastic Thomson scattering. The radiation corrected for the dark background and scattered by the material system i at the scattering vector $\vec{q}$, measured in counts per second, can be expressed by

$$I_\mathrm{i}(\vec{q}) = C \cdot I_0 \cdot T_\mathrm{i} \cdot V_\mathrm{i} \cdot \Delta\Omega \cdot \eta \cdot \left(\frac{\mathrm{d}\sigma}{\mathrm{d}\Omega}\right)_\mathrm{i}(\vec{q}), \tag{1}$$

where C is a dimensionless calibration constant that must be determined for the measurement setup and measurement conditions such as the sample-to-detector distance respectively. I_0 is the incident beam in counts per time and area. The transmission T_i is the ratio of the integral intensity measured at the detector in the region of the primary beam with the sample to that without the sample. The illuminated sample volume V_i can be evaluated by

$$V_\mathrm{i} = A \cdot l_\mathrm{i}, \tag{2}$$

where A is the beam cross-section and l_i the sample thickness, which is a measure of the depth that the beam must penetrate. Since the scattered radiation propagates radially from the scattering center, the intensity of the scattered radiation is normalized to the solid angle $\Delta\Omega$. η is the detector efficiency. The last factor in Eq. (1) is referred to as the macroscopic scattering cross-section in cm^{-1}, also known as the intensity in absolute units, as it is characteristic for a specific sample and independent of the measurement conditions. If the sample is a loose powder, a precise evaluation of the sample thickness is hardly accessible, as it can vary from measurement to measurement. Therefore, it is initially more practical to normalize the measured intensity units $I_\mathrm{i}(\vec{q})$ only by the irradiated cross-sectional area A instead of the sample volume V_i. The resulting intensity units, in the following referred to as the length-scaled macroscopic scattering cross-section, will thus retain the information of the sample thickness. Combining (1) and (2) the length-scaled macroscopic scattering cross-section is given by

$$\left(\frac{\mathrm{d}\Sigma}{\mathrm{d}\Omega}\right)_\mathrm{i}(\vec{q}) := l_\mathrm{i}\left(\frac{\mathrm{d}\sigma}{\mathrm{d}\Omega}\right)_\mathrm{i}(\vec{q}) = \frac{I_\mathrm{i}(\vec{q})}{C \cdot I_0 \cdot T_\mathrm{i} \cdot A \cdot \Delta\Omega \cdot \eta}, \tag{3}$$

and it describes the scattering contribution of the total mass of the particle type in the sample. In a loose powder, an effective length, the solid thickness l_eff, can be chosen as the sample thickness. The solid thickness can be determined when the sample transmission is known and evaluated using the Lambert-Beer law according to

$$l_\mathrm{eff,\,i} = \frac{-\ln T_\mathrm{i}}{\mu_\mathrm{i}}, \tag{4}$$

where μ_i is the total absorption coefficient that accounts for all attenuation effects, including elastic and inelastic scattering as well as photoabsorption. These rescaled intensity units are called effective intensity units and, for the material system i, can be evaluated by

$$I_\mathrm{eff,i}(\vec{q}) = \frac{1}{l_\mathrm{eff,\,i}}\left(\frac{\mathrm{d}\Sigma}{\mathrm{d}\Omega}\right)_\mathrm{i}(\vec{q}), \tag{5}$$

where $l_\mathrm{eff,i}$ and the length-scaled macroscopic scattering-cross-section are accessible from the transmission measurement and SAXS measurement. For further information concerning the normalization to effective intensities the reader might refer to (Spalla et al., 2003). In a sample containing multiple particle types, each particle type contributes to the total intensity of a measurement. Approximatively, the measured total length-scaled macroscopic scattering cross-section is the sum of the length-scaled macroscopic scattering cross-sections of the individual components. This assumption is justified by neglecting interparticle interactions, whose influence depends on the considered scattering vector range and particle size. In this work, we focus on large scattering vectors within the Porod region, where the structure factor can be neglected. The intensity is now to be presented in such a way that from the measurable intensity on the detector, which includes the scattering contributions of all particle types, the effective intensities of all particle types can be derived.

Starting from Eq. (3) one obtains

$$\frac{I_\mathrm{Mix}(\vec{q})}{C \cdot I_0 \cdot T_\mathrm{Mix} \cdot A \cdot \Delta\Omega \cdot \eta} = \sum_{\mathrm{i}=1}^{N}\left(\frac{\mathrm{d}\Sigma}{\mathrm{d}\Omega}\right)_\mathrm{i}(\vec{q}), \tag{6}$$

where $I_\mathrm{Mix}(\vec{q})$ is the measurable intensity on the detector and represents the intensity scattered by the particle mixture in counts per second given by

$$I_\mathrm{Mix}(\vec{q}) = T_\mathrm{Mix}\sum_{\mathrm{i}=1}^{N}\frac{I_\mathrm{i}(\vec{q})}{T_\mathrm{i}}. \tag{7}$$

The transmission of the particle mixture T_{Mix} results from the attenuation caused by each individual component within the powder and is a product of each contribution given by

$$T_{\mathrm{Mix}} = \prod_{\mathrm{i}=1}^{N} T_{\mathrm{i}} \tag{8}$$

Since all quantities on the left-hand side of Eq. (6) are known in a SAXS measurement, the measurement (M) of a mixture of material i and material j will directly be expressed in terms of the length-scaled macroscopic scattering cross-section and be referred to as follows:

$$\left(\frac{\mathrm{d}\Sigma}{\mathrm{d}\Omega}\right)_{\mathrm{i+j}}^{(\mathrm{M})}(\vec{q}) = \left(\frac{\mathrm{d}\Sigma}{\mathrm{d}\Omega}\right)_{\mathrm{i}}^{(\mathrm{M})}(\vec{q}) + \left(\frac{\mathrm{d}\Sigma}{\mathrm{d}\Omega}\right)_{\mathrm{j}}^{(\mathrm{M})}(\vec{q}). \tag{9}$$

At this point, it is important to note again that the length-scaled macroscopic scattering cross-section is proportional to the sample thickness, making the declaration of the measurement in brackets crucial. If the same particle system is measured twice using two samples of one powder, the sample thickness will generally differ, resulting in variations in the length-scaled macroscopic scattering cross-section. After normalizing for the solid thickness, the results become comparable.

Once the effective intensity of a component $I_{\mathrm{eff,i}}$ is known, the intensity for a smooth surface will follow Porod's law for $q \to \infty$, as described by:

$$I_{\mathrm{eff,i}} = K_{P,\mathrm{i}} \cdot q^{-4}. \tag{10}$$

The Porod Constant $K_{P,\mathrm{i}}$ is related to the specific surface area of the sample and can be evaluated by fitting Eq. (10) to the experimental data. The specific surface area of the particle system i is given by

$$S_{\mathrm{V}} = \frac{K_{P,\mathrm{i}}}{2\pi\Delta\rho_{sl}^{2}}, \tag{11}$$

where $\Delta\rho_{sl}$ ($\mathrm{Å}^{-2}$) represents the difference in scattering length density across the solid interface (Glatter and Kratky, 1983).

3. Experimental setup and reactor design

The experimental setup comprises two major elements: a laboratory-scale reduction unit with optical access for X-ray radiation and a laboratory-scale beamline for X-ray scattering experiments.

3.1. Reduction unit and operating conditions

The reduction system comprises a mass flow controller (MFC, Wagner Mess- und Regeltechnik GmbH, Offenbach am Main, Germany), two pressure sensors (BD SENSORS GmbH, Thierstein, Germany), a capillary enclosed by a heating cell with an optical window (Linkam Scientific Instruments Ltd., Salfords, United Kingdom) and a temperature sensor (TC Mess- und Regeltechnik GmbH, Mönchengladbach, Germany).

The MFC regulates a standard volumetric flow of forming gas (2 % H_2 in N_2) within a range of 0 to 50 $\mathrm{mL_n/min}$, serving as the inflow into the capillary. Due to the significant pressure losses associated with the flow through the packed bed, a pressure p_1 develops upstream of the bed, which is monitored using a primary pressure sensor. The second pressure sensor measures the gas pressure p_2 after the flow has passed through the packed bed, after the capillary. The heating cell can be controlled up to 350°C via an internal regulation system. Additionally, behind the packed bed, the temperature of the gas T after passing through the bed is measured using a temperature sensor located in the capillary. Fig. 1 depicts a schematic diagram of the experimental setup for the reduction unit.

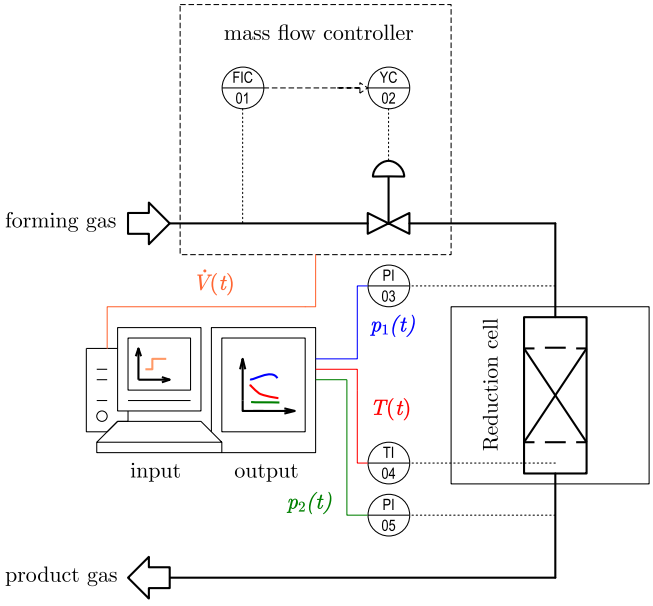

Fig. 1. Schematic representation of the experimental setup for ensuring defined reaction conditions for the iron oxide reduction.

3.2. Reactor design and material

The reaction is carried out in a small borosilicate glass capillary (Hilgenberg GmbH, Malsfeld, Germany) with an inner diameter of $d_{\mathrm{cap,i}} = 0.918\,\mathrm{mm}$. The powder sample, comprising reactive iron oxide (FeOx) particles and inert boron nitride (BN) particles, is placed between quartz wool layers (Carl Roth GmbH + Co. KG, Karlsruhe, Germany) to stabilize its position within the capillary. The BN particles (Sigma-Aldrich Chemie GmbH, Taufkirchen, Germany), with an average diameter of $d_{50,\mathrm{BN}} = 13.65\,\mu\mathrm{m}$ as determined by laser diffraction, are used as an attenuation-optimizing solid particle system. To ensure sufficient transmission values for X-ray measurements, various mass ratios of BN and FeOx were tested. As a result, a mass ratio of $w_{\mathrm{FeOx,0}} : w_{\mathrm{BN,0}} = 3 : 7$ is selected ensuring high transmission while maintaining a sufficient XRD signal from the FeOx particles.

The *initial* solid bed for each reduction experiment is composed of reactive Fe_2O_3 particles (Sigma-Aldrich Chemie GmbH, Taufkirchen, Germany) with a mean diameter $d_{50,\mathrm{Fe_2O_3}} = 1.46\,\mu\mathrm{m}$, embedded within the aforementioned inert BN powder. Since oxygen is continuously removed from the oxide phase during the iron oxide reduction, the mass and, thus, the volume of the FeOx particles decrease over the reaction progress.

3.3. Experimental setup for X-ray scattering experiments

Each X-ray scattering measurement was conducted in the laboratory-scale SWAXS beamline Xeuss 2.0 Q-Xoom (Xenocs SA, Grenoble, France). The used measurement device mainly consists of an X-ray microfocus source (Genix3D Cu ULC) that emits Cu – K_α radiation, a collimation system, an evacuatable sample chamber and a hybrid pixel detector (Pilatus3 R 300k, Dectris Ltd., Baden-Dättwil, Switzerland). The collimated X-ray beam with an energy of 8.04 keV irradiates the sample within the reactor setup by passing through the optical window. The beam cross-section was set to 500 µm x 500 µm to ensure that it did not exceed the inner edges of the capillary while irradiating a sufficiently large amount of powder. The distance between the powder sample within the capillary and the detector is set to 1000 mm for SAXS measurements and 79.2 mm for WAXS measurements. A schematic representation of the reduction cell for the simultaneous collection of SAXS and WAXS data is depicted in Fig. 2.

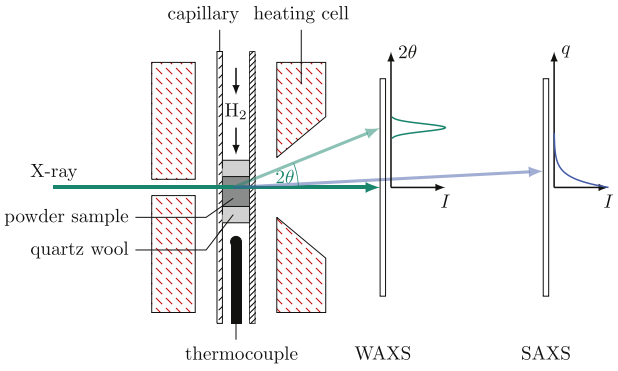

Fig. 2. Schematic representation of the reactor setup for the collection of SAXS and WAXS scattering data without removing the powder from the reaction setup.

4. Methods and data treatment

4.1. Calibration of effective intensities

To obtain absolute and effective intensities from a SAXS measurement, the calibration factor C in Eq. (1) must be determined. Therefore, pure water within the reactor will be employed as a calibration standard. The theoretical differential scattering cross-section of water can be calculated using

$$\left(\frac{\mathrm{d}\sigma}{\mathrm{d}\Omega}\right)^{(\mathrm{th})}_{\mathrm{H_2O}}(\vec{q}) = \rho^2_{sl,\mathrm{H_2O}}\, kT\, \beta_T, \tag{12}$$

where k is the Boltzmann constant, T is the temperature and β_T is the isothermal compressibility of water under the measurement conditions. For 25 °C the absolute intensity of water can be evaluated as $0.0166\,\mathrm{cm^{-1}}$.

The measurement (C) of the empty reactor (referred to as the 'cell') provides

$$\left(\frac{\mathrm{d}\Sigma}{\mathrm{d}\Omega}\right)^{(\mathrm{C})}_{\mathrm{cell}}(\vec{q}) = \frac{I_{\mathrm{cell}}(\vec{q})}{C \cdot I_0 \cdot T_{\mathrm{cell}} \cdot A \cdot \Delta\Omega \cdot \eta}. \tag{13}$$

The measurement (S) of the standard within the cell can be described as

$$\left(\frac{\mathrm{d}\Sigma}{\mathrm{d}\Omega}\right)^{(\mathrm{S})}_{\mathrm{H_2O}}(\vec{q}) + \left(\frac{\mathrm{d}\Sigma}{\mathrm{d}\Omega}\right)^{(\mathrm{S})}_{\mathrm{cell}}(\vec{q}) = \frac{I_{\mathrm{H_2O+cell}}(\vec{q})}{C \cdot I_0 \cdot T_{\mathrm{H_2O}} T_{\mathrm{cell}} \cdot A \cdot \Delta\Omega \cdot \eta}. \tag{14}$$

With measured sample transmissions of $T^{(\mathrm{C})} = 0.489$ and $T^{(\mathrm{S})} = T_{\mathrm{H_2O}} T_{\mathrm{cell}} = 0.2283$, the resulting transmission of pure water in the beam is $T_{\mathrm{H_2O}} = 0.4671$. The thickness of the sample corresponds to the pure thickness of the water, which is evaluated according to Eq. (4). This results in an effective thickness of $l_{\mathrm{eff,H_2O}} = 0.775$ mm. Based on the condition

$$\left(\frac{\mathrm{d}\sigma}{\mathrm{d}\Omega}\right)^{(\mathrm{th})}_{\mathrm{H_2O}}(\vec{q}) = \frac{1}{l_{\mathrm{eff}}}\left[\left(\frac{\mathrm{d}\Sigma}{\mathrm{d}\Omega}\right)^{(\mathrm{S})}_{\mathrm{H_2O}}(\vec{q}) + \left(\frac{\mathrm{d}\Sigma}{\mathrm{d}\Omega}\right)^{(\mathrm{S})}_{\mathrm{cell}}(\vec{q}) - \left(\frac{\mathrm{d}\Sigma}{\mathrm{d}\Omega}\right)^{(\mathrm{C})}_{\mathrm{cell}}(\vec{q})\right] \tag{15}$$

the calibration factor can then be calculated using

$$C = \frac{\frac{I_{\mathrm{H_2O+cell}}(\vec{q})}{I_0 \cdot T_{\mathrm{H_2O}} T_{\mathrm{cell}} \cdot A \cdot \Delta\Omega \cdot \eta} - \frac{I_{\mathrm{cell}}(\vec{q})}{I_0 \cdot T_{\mathrm{cell}} \cdot A \cdot \Delta\Omega \cdot \eta}}{\left(\frac{\mathrm{d}\sigma}{\mathrm{d}\Omega}\right)^{(\mathrm{th})}_{\mathrm{H_2O}}(\vec{q})} = 1.31. \tag{16}$$

4.2. Analysis of the phase composition by WAXS

The scattering curves obtained from wide-angle scattering experiments are, similarly to XRD results, presented as intensity I plotted against the scattering angle 2θ. The objective is to determine the mass fraction of each iron oxide (and iron) species within the FeOx particles. Quantitative analysis in this work relies on the intensity ratio method, which was calibrated specifically for the reactor as the sample holder. In previous work (Buchheiser et al., 2023), this method was described in detail and applied to determine the phase composition of flame-oxidized iron oxide particles. Sperling et al. (2025) further validated this method by comparing its results to those obtained from Mössbauer spectroscopy. For a comprehensive description of the quantitative phase analysis, readers are referred to the aforementioned previous studies.

4.3. Material property evaluation

To interpret the SAXS measurement results, the mass density, total absorption, and scattering contrast of the powder must be known. Since the powder contains two different particle types, BN and FeOx, with the latter potentially comprising several iron oxide species, this section will thoroughly describe the methodology used to determine the material properties.

As described in Section 4.2, the mass fraction of each iron/ iron oxide species within the metal oxide particles can be determined. Since the mass densities and molar masses of the iron oxide components are well known, the molar fraction and volume fraction of each species i can be evaluated using Eq. (17) and (18):

$$z_{\mathrm{i}} = \frac{\frac{w_{\mathrm{i}}}{M_{\mathrm{i}}}}{\sum_{\mathrm{j}=1} \frac{w_{\mathrm{j}}}{M_{\mathrm{j}}}}, \tag{17}$$

$$\phi_{\mathrm{i}} = \frac{\frac{w_{\mathrm{i}}}{\rho_{\mathrm{i}}}}{\sum_{\mathrm{j}=1} \frac{w_{\mathrm{j}}}{\rho_{\mathrm{j}}}}. \tag{18}$$

While the mass of iron within the FeOx particles remains constant during the iron oxide reduction, the amount of oxygen decreases. Therefore, the stoichiometry of FeOx depends on the reduction time and can be expressed as

$$x = \frac{3z_{\mathrm{Fe_2O_3}} + 4z_{\mathrm{Fe_3O_4}} + z_{\mathrm{FeO}}}{2z_{\mathrm{Fe_2O_3}} + 3z_{\mathrm{Fe_3O_4}} + z_{\mathrm{FeO}} + z_{\mathrm{Fe}}}, \tag{19}$$

so that the reduction degree from hematite to iron in a full conversion shall be defined as

$$\chi(t) = \frac{1.5 - x(t)}{1.5}. \tag{20}$$

Furthermore, the ratio of particle mass to a fully reduced reference particle can then be formulated as

$$\xi(t) = \frac{u_{\mathrm{Fe}} + x(t) \cdot u_{\mathrm{O}}}{u_{\mathrm{Fe}}}, \tag{21}$$

where u_{Fe} and u_{O} are the atomic masses of iron and oxygen, respectively. Thus, based on the mass ratios of metal oxide and BN ($w_{\mathrm{Ox},0}$, $w_{\mathrm{BN},0}$) within the reactor at time t_0, the ratio of metal/metal oxide particles to BN particles within the bulk material can be evaluated at any given time t:

$$w_{\mathrm{Ox}}(t) = \left[\frac{\xi(t_0)}{\xi(t)}\left(\frac{1}{w_{\mathrm{Ox},0}} - 1\right) + 1\right]^{-1}. \tag{22}$$

Since all fractions can be determined using the WAXS measurements, the material properties of the reactive FeOx particles in the bulk material can also be provided at any given time. The average mass density of the FeOx particles within the powder can directly be calculated using

$$\rho_{\mathrm{FeOx}} = \left(\sum_{\mathrm{i}=1}^{N} \frac{w_{\mathrm{i}}}{\rho_{\mathrm{i}}}\right)^{-1}. \tag{23}$$

The average total absorption coefficient μ_{FeOx} is provided by

$$\mu_{\mathrm{FeOx}} = \rho_{\mathrm{FeOx}}\, \frac{u_{\mathrm{Fe}} \cdot \tilde{\mu}_{\mathrm{Fe}}(\lambda) + x(t) \cdot u_{\mathrm{O}} \tilde{\mu}_{\mathrm{O}}(\lambda)}{u_{\mathrm{Fe}} + x(t) \cdot u_{\mathrm{O}}}, \tag{24}$$

where $\tilde{\mu}_{\mathrm{Fe}}(\lambda)$ and $\tilde{\mu}_{\mathrm{O}}(\lambda)$ represent the respective mass specific total absorption coefficients of the elements for the given wavelength of the X-ray radiation. The average scattering length density of the FeOx particles is given by

$$\rho_{sl,\mathrm{FeOx}} = r_0\, N_A\, \rho_{\mathrm{FeOx}}\, \frac{f'_{\mathrm{Fe}}(\lambda) + x(t) \cdot f'_{\mathrm{O}}(\lambda)}{M_{\mathrm{Fe}} + x(t) \cdot M_{\mathrm{O}}}, \tag{25}$$

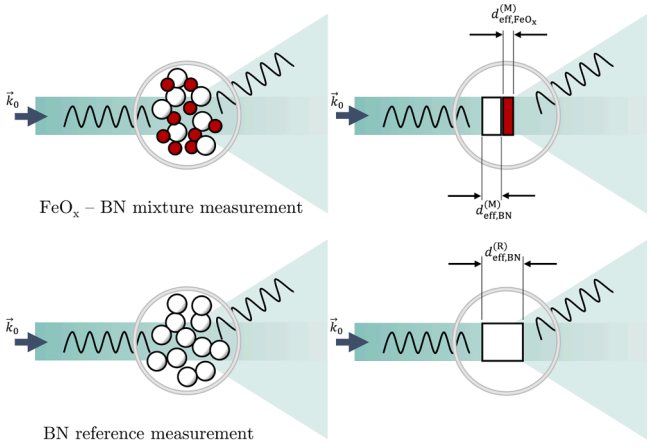

Fig. 3. Schematic representation of the effective solid thicknesses in the FeOx – BN particle mixture $d^{(M)}_{eff,FeOx}$ and $d^{(M)}_{eff,BN}$ and in the BN reference $d^{(R)}_{eff,BN}$.

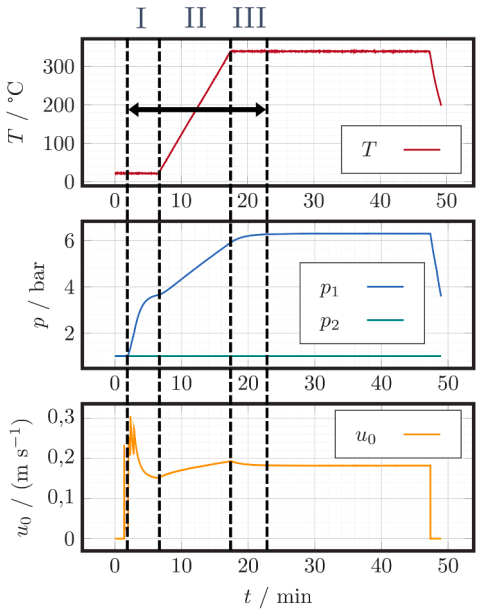

Fig. 4. Start-up phases and heating of the reactor to reaction temperature: **I Cold Startup Phase** Establishing pressure until a steady-state level is reached at ambient temperature, **II Heating Phase** Achieving end temperature within the reactor, **III Relaxation Phase** Reaching steady-state conditions.

where $r_0 = 2.17940 \cdot 10^{-15}$m is the classical electron radius, N_A is the Avogadro's number and $f'_{Fe}(\lambda)$ and $f'_O(\lambda)$ are the atomic scattering factors. The scattering contrast between the FeOx particles within the powder and their environment is estimated to be

$$\Delta\rho_{sl} = \rho_{sl,FeOx} - \rho_{e,env} \approx \rho_{sl,FeOx} \tag{26}$$

as the measurements are conducted under vacuum conditions, with only point contacts occurring between the BN and FeOx particles. It should be noted that the averaged scattering length density of the particles does not accurately describe the scattering contrast along the particle surface. This is due to the non-homogeneous radial composition distribution that develops during the reaction. The surface-near region of the particle is expected to contain less oxygen compared to the region near the particle center. To account for this variation, the scattering length density contrast will be evaluated using the core-shell model of iron reduction, which assumes that the outermost exposed surface consists of the most reduced phase present and identified by WAXS. An error estimation is given in Section 4.7.

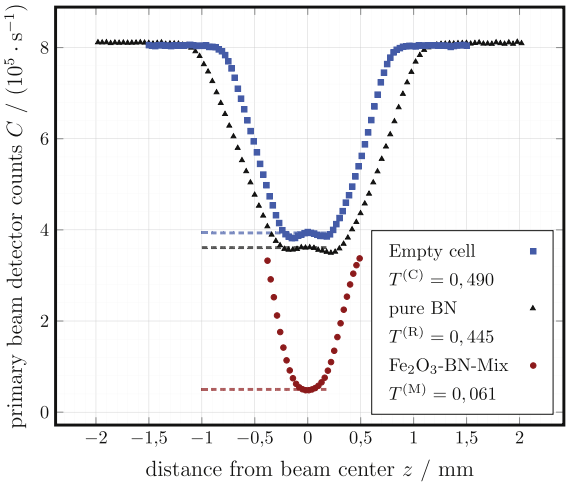

Fig. 5. Representation of primary beam intensity curves for determining sample transmission: intensity curves for an empty reactor, a reactor filled with boron nitride, and a reactor filled with the reaction mixture hematite - boron nitride.

Table 1
Representation of the evolution of the determined specific surface areas during the thermochemical reduction of hematite particles.

Pure material	S_V/(m^2 cm^{-3})
$\chi = 0$	15.2 ± 0.74
$\chi = 0.11$	16.1 ± 0.54
$\chi = 1$	18.0 ± 0.82

Table 2
Mass specific total absorption coefficient and atomic scattering factors of the elements used for evaluating the material properties of the FeOx particles and BN particles for $\lambda = 1.5406$ Å based on (Seltzer, 1995a,b).

Element i	$\tilde{\mu}_i(\lambda)$/(cm^2 g^{-1})	$f'(\lambda)$/−
Fe	300.698	24.83089
O	11.006	8.052019
B	2.195	-
N	7.189	-

Table 3
Mass densities of the pure solid phases identified in the powder samples based on Haynes et al. (2017).

Pure material	ρ/(g cm^{-3})
α–Fe	7.87
FeO	6.0
Fe_3O_4	5.17
Fe_2O_3	5.25
BN	2.18

4.4. Specific surface evaluation in a multi-particle system

Within the reactor, there are BN particles serving as attenuation-optimizing particles and FeOx particles acting as the reacting particles. The specific surface information of only the FeOx particles must be extracted from the data. To achieve this, three preliminary measurements must be performed: the empty camera measurement (E), the empty cell

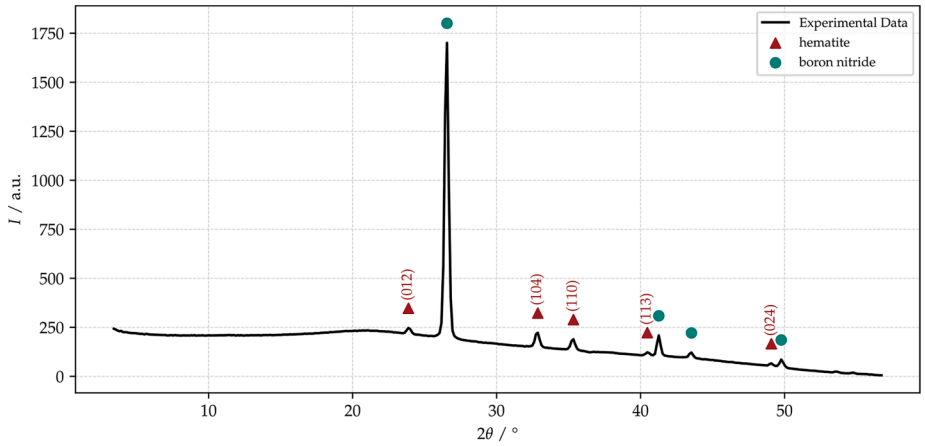

(a) $\chi = 0$

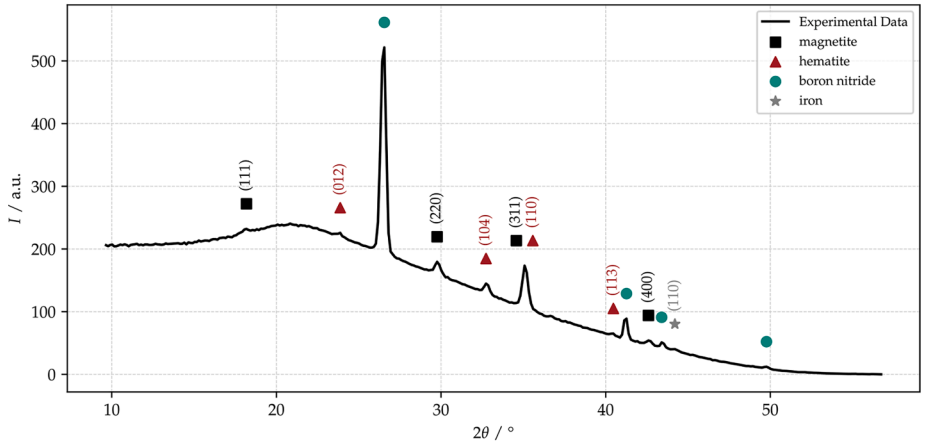

(b) $\chi = 0.11$

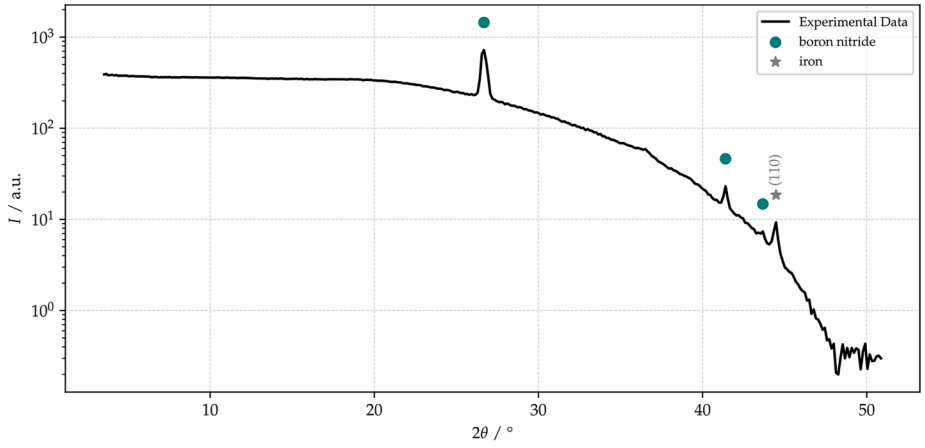

(c) $\chi = 1$

Fig. 6. Representation of the WAXS scattering curves for three different reduction degrees for the reduction of hematite at 350 °C.

measurement (C), and the reactor filled exclusively with BN particles as a reference (R). Once these measurements are completed, the reactor filled with FeOx particles is measured for each time step, referred to as the mixture measurements (M). While the length-scaled macroscopic scattering cross-section of the cell remains constant across all measurements, the length-scaled macroscopic scattering cross-section of the BN particles in (M) and (R) may vary due to differences in the solid thickness of BN within the cell. As a result, the length-scaled macroscopic scattering cross-section of BN must be rescaled accordingly:

$$\left(\frac{\mathrm{d}\Sigma}{\mathrm{d}\Omega}\right)_{\mathrm{BN}}^{(\mathrm{M})}(\vec{q}) = \frac{d_{\mathrm{eff,\,BN}}^{(\mathrm{M})}}{d_{\mathrm{eff,\,BN}}^{(\mathrm{R})}}\left(\frac{\mathrm{d}\Sigma}{\mathrm{d}\Omega}\right)_{\mathrm{BN}}^{(\mathrm{R})}(\vec{q}). \tag{27}$$

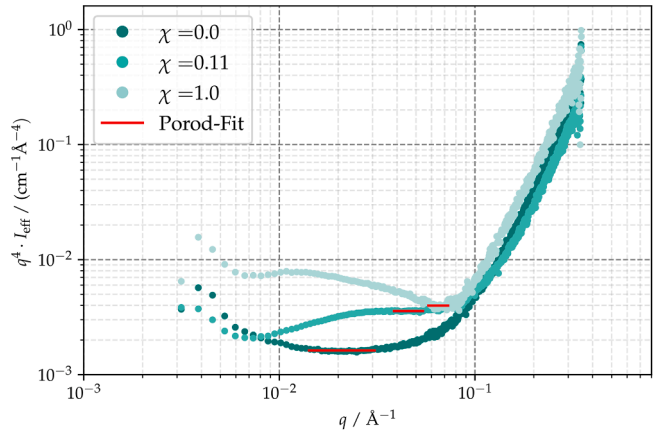

Fig. 7. SAXS scattering curves (Porod plot) for three reduction degrees during the reduction of hematite at 350 °C, showing the evolution of the Porod regions.

Thus, the effective intensity of FeOx within the reactor can be expressed as

$$I_{\mathrm{eff,FeOx}}(\vec{q}) = \frac{1}{d^{(\mathrm{M})}_{\mathrm{eff,FeOx}}} \left[\left(\frac{\mathrm{d}\Sigma}{\mathrm{d}\Omega} \right)^{(\mathrm{M})}_{\mathrm{FeOx+BN}} (\vec{q}) - \left(\frac{\mathrm{d}\Sigma}{\mathrm{d}\Omega} \right)^{(\mathrm{M})}_{\mathrm{BN}} (\vec{q}) \right], \tag{28}$$

with

$$\left(\frac{\mathrm{d}\Sigma}{\mathrm{d}\Omega} \right)^{(\mathrm{M})}_{\mathrm{FeOx+BN}} (\vec{q}) = \left[\left(\frac{\mathrm{d}\Sigma}{\mathrm{d}\Omega} \right)^{(\mathrm{M})}_{\mathrm{FeOx+BN+cell}} (\vec{q}) - \left(\frac{\mathrm{d}\Sigma}{\mathrm{d}\Omega} \right)^{(\mathrm{C})}_{\mathrm{cell}} (\vec{q}) \right] \tag{29}$$

and

$$\left(\frac{\mathrm{d}\Sigma}{\mathrm{d}\Omega} \right)^{(\mathrm{M})}_{\mathrm{BN}} (\vec{q}) = \frac{d^{(\mathrm{M})}_{\mathrm{eff,\,BN}}}{d^{(\mathrm{R})}_{\mathrm{eff,\,BN}}} \left[\left(\frac{\mathrm{d}\Sigma}{\mathrm{d}\Omega} \right)^{(\mathrm{R})}_{\mathrm{BN+cell}} (\vec{q}) - \left(\frac{\mathrm{d}\Sigma}{\mathrm{d}\Omega} \right)^{(\mathrm{C})}_{\mathrm{cell}} (\vec{q}) \right]. \tag{30}$$

To evaluate Eq. (28) the effective solid thicknesses of BN in the mixture $d^{(\mathrm{M})}_{\mathrm{eff,BN}}$ and in the BN reference $d^{(\mathrm{R})}_{\mathrm{eff,BN}}$ as well as the effective solid thickness of the FeOx particles $d^{(\mathrm{M})}_{\mathrm{eff,FeOx}}$ in the mixture must be known. In the BN reference measurement, the effective solid thickness can be determined directly by evaluating the transmission values of the cell (C) and the reference (R) according to:

$$d^{(\mathrm{R})}_{\mathrm{eff,BN}} = -\frac{1}{\mu_{\mathrm{BN}}} \cdot \ln \frac{T^{(\mathrm{R})}}{T^{(\mathrm{C})}}. \tag{31}$$

To evaluate $d^{(\mathrm{M})}_{\mathrm{eff,FeOx}}$ $d^{(\mathrm{M})}_{\mathrm{eff,BN}}$ the volume fractions ϕ_{FeOx} and ϕ_{BN} of FeOx and BN must be determined using the WAXS measurement for the determination of the mass fractions of the oxide phases within the FeOx particles and the help of Eqs. (17), (18), (19), (21) and (22). Consequently, the effective solid thickness of FeOx in the measurement of the mixture is given by

$$d^{(\mathrm{M})}_{\mathrm{eff,FeOx}} = -\frac{1}{\mu_{\mathrm{FeOx}} + \frac{\phi^{(\mathrm{M})}_{\mathrm{BN}}}{1-\phi^{(\mathrm{M})}_{\mathrm{BN}}} \cdot \mu_{\mathrm{BN}}} \cdot \ln \frac{T^{(\mathrm{M})}}{T^{(\mathrm{C})}}, \tag{32}$$

the effective solid thickness of BN in the mixture measurement is provided by

$$d^{(\mathrm{M})}_{\mathrm{eff,BN}} = \frac{\phi^{(\mathrm{M})}_{\mathrm{BN}}}{1-\phi^{(\mathrm{M})}_{\mathrm{BN}}} \cdot d^{(\mathrm{M})}_{\mathrm{eff,FeOx}}. \tag{33}$$

A schematic representation of the evaluated effective solid thicknesses is depicted in Fig. 3. As a result of this, the specific surface of the FeOx particles within the reactor can be calculated using Eq. (10), (11) and (28).

4.5. Reduction experiment and ramp-up process

Each reduction experiment consisted of the three following steps:

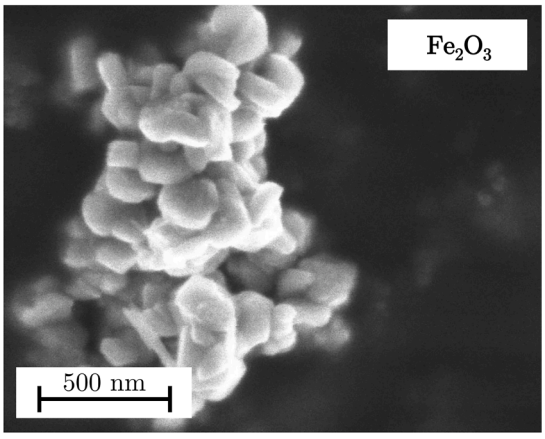

(a) hematite particle

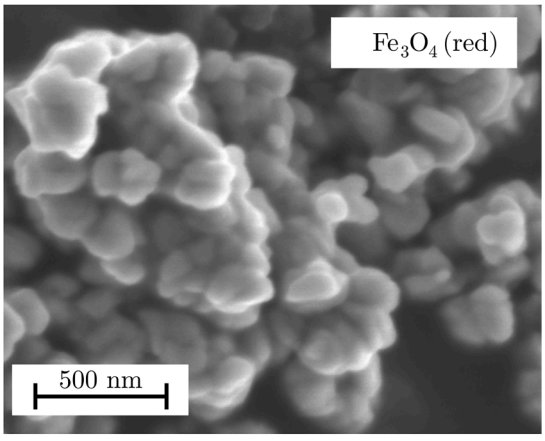

(b) particle at the intermediate stage

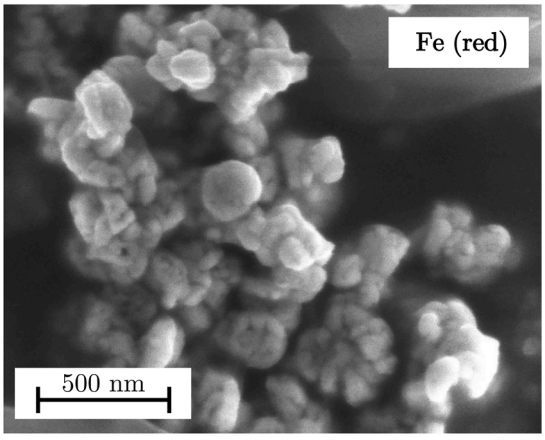

(c) fully reduced particle

Fig. 8. Comparison of the particle morphology between a) an arbitrarily chosen hematite particle (reactant) before reduction , b) an arbitrarily chosen particle at the intermediate stage and c) an arbitrarily chosen iron particle (product) after the complete reduction of hematite. To sample a particle at the intermediate stage, the experiment was repeated under the same conditions.

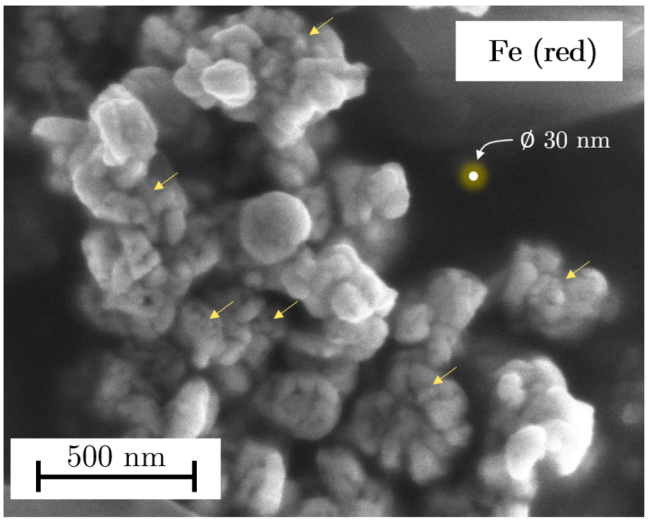

Fig. 9. Enlarged view of an iron particle after reduction, highlighting the nanostructures ≤ 30 nm formed. The arrows indicate regions where structuring at these size scales becomes apparent.

1. System ramp-up until steady-state conditions are reached
2. Reduction period
3. System shut down and conduction of the scattering measurements

The system ramp-up itself comprised three phases. Initially, the mass flow through the reactor was increased to operating conditions at ambient temperatures (cold startup phase). Once the pressure upstream of the packed bed became nearly constant, the stage was heated to the reaction temperature (350 °C) at a heating rate of approximately 30 K min^{-1} (heating phase). After the target temperature was reached, a significant pressure drop developed, causing an increase in the upstream pressure before the reactor. Consequently, the superficial gas velocity slightly decreased until steady-state conditions were achieved (relaxation phase). To minimize the impact of the startup process, the startup time for each measurement point is kept below 5 % of the total duration of the reduction period. The shutdown and cooling time could be kept even shorter due to the small geometric dimensions of the capillary. The sample was directly evacuated in the sample chamber after the reaction, and SAXS and WAXS measurements were conducted at pressures below 1 mbar.

The time required to reach steady state conditions in the capillary and during cooling defines the temporal resolution of the technique. The SWAXS measurement device, however, has only a minor impact. Thus, fast structural changes or temperature effects can only be observed using time-resolved in-situ analysis.

4.6. Transmission evaluation

To determine the average solid thicknesses within the sample, it is necessary to measure the sample's transmission. Therefore, to measure the transmitted radiation, the capillary was gradually shifted within the beam while determining the intensity in counts per second across all pixels within the primary beam's area. This process ensured alignment of the capillary's center, at which point the intensity of the transmitted radiation is recorded. Once the capillary fully exits the primary beam's area, the intensity of the incident beam I_0 can be approximately determined. The transmission equals the ratio of both intensity values. The alignment curves for determining the transmission values of the empty capillary, the capillary filled with boron nitride, and the capillary containing the reactant sample are shown in Fig. 5. This procedure has been applied in order to align the capillary for each SAXS measurement.

4.7. Uncertainty estimation

In this work, the error estimation in the quantification of the specific surface area accounts for the two factors: first, the uncertainty associated with the Porod fit to the experimental SAXS data, and second, the error arising from the estimation of the scattering length density using the core-shell model during the reduction process. The error estimation for the conversion into effective intensities as well as for the determination of the transmission is not considered in this study.

The uncertainty of the specific surface area based on Eq. (11) is evaluated by

$$\sigma_{S_V}^2 = \left(-2\frac{K_P}{2\pi}\Delta\rho_{sl}^{-3}\right)^2 \cdot \sigma_{\Delta\rho_{sl}}^2 + \left(\frac{1}{2\pi}\Delta\rho_{sl}^{-2}\right)^2 \cdot \sigma_{K_P}^2, \tag{34}$$

where σ_{K_P} is the uncertainty from fitting K_P to the experimental data. This uncertainty is estimated from

$$\sigma_{K_P}^2 \leq q_{\max}^4 \cdot \sigma_I^2, \tag{35}$$

where $q_{\max}$ is the maximum q value of the fitting range and σ_I the standard deviation between experimental data points and Porod fit.

The literature values for the scattering length densities are $4.12 \cdot 10^{-5}$ $Å^{-2}$ for Fe_2O_3, $4.04 \cdot 10^{-5}$ $Å^{-2}$ for Fe_3O_4 and $5.94 \cdot 10^{-5}$ $Å^{-2}$ for Fe respectively. The uncertainty is estimated as $\sigma_{\Delta\rho_{sl}} = 0.1 \cdot 10^{-5}$ $Å^{-2}$.

5. Results and discussion

5.1. WAXS Analysis

The WAXS results are used to quantify the phases present within the FeOx particles, thereby providing information on the reduction degree χ and material properties. Fig. 6 exemplarily shows three WAXS curves: a) the state of the hematite - boron nitride mixture before the reaction, b) an intermediate state after the onset of reduction where all phases coexist, and c) the state of the reaction mixture after complete conversion.

In all diffractograms, the wide-angle range is resolved up to approximately 50°. Fig. 6 a) specifies all hematite peaks retrieved from the educt sample measurement. After the onset of the reduction process, the (104) hematite peak at a scattering angle of 33.17° diminishes while the magnetite (220) peak at a scattering angle of 30.36° grows correspondingly. As can be seen in Fig. 6 b), the reaction proceeds in such a way that hematite is initially converted to magnetite. The mass fraction of hematite is approximately 28 %, that of magnetite is 70 %, a small amount of formed iron (2 %) is also present in the sample, since the (110) α-iron peak at a scattering angle of 44.69° can be observed. The diffractogram of the full reduction to iron in Fig. 6 c) does only contain the boron nitride peaks and the (110) α-iron peak. To emphasize the peaks at scattering angles above 40°, a logarithmic scaling of the intensity axis is applied here. This is necessary because, in all diffractograms, it is evident that the baseline intensity level decreases significantly at higher scattering angles as the scattering angle increases. This decrease is attributed to the geometric arrangement of the optical window and the embedding of the capillary within the heating unit. When the beam passes through the capillary, radiation scattered at large angles can only reach the detector if the scattering occurs near the exit point. However, proper embedding of the capillary within the heating element turned out to be essential to ensure a nearly constant temperature throughout the capillary. Thus, the effect on the quantitative phase analysis was taken into account and corrected through an adapted calibration using the intensity ratio method.

5.2. SAXS Analysis

Fig. 7 displays the Porod plot of the SAXS curves of the FeOx particles corresponding to the measurements discussed in Section 5.1. In this form of representation, the intensity curve in the Porod regime appears

horizontal according to Eq. (10). Using Eq. (11), the specific surface area is then evaluated. It can be observed that the specific surface area of the solid particles increases with the reduction degree, from approximately $15.2\,m^2\,cm^{-3}$ at $\chi = 0$ to $18\,m^2\,cm^{-3}$ at $\chi = 1$ after the reduction is complete. The results are summarized in Table 1. Interestingly, the Porod fits not only reach higher intensity levels with increasing reduction degree, but also the scattering vector range shifts to higher values. Thereby, it is noteworthy that with an increasing reduction degree, additional scattering contributions in the scattering vector range between $0.01\,Å^{-1}$ and $0.06\,Å^{-1}$ emerge. Since the SAXS curve for scattering vectors $> |\vec{q}_1|$ provides all the information of structures with the largest diameter of $d_{eq} = \pi/|\vec{q}_1|$ (Glatter and Kratky, 1983), the information of structures with equivalent sizes of up to approximately 30 nm can be derived from the measured data in this scattering vector range. It can be evaluated that the SAXS curves of $\chi = 0.11$ and $\chi = 1$ differ in that the additional scattering contribution compared to the hematite scattering curve ($\chi = 0$) tends to originate from smaller structures at larger scattering vectors ($0.04 - 0.06\,Å^{-1}$), while in $\chi = 1$, additional scattering contributions arise at smaller scattering vectors ($0.01 - 0.03\,Å^{-1}$) from larger structures. This indicates an additional scattering contribution arising from nanostructures up to size scales of 30 nm in the resolved scattering range.

5.3. SEM Analysis

To further validate the morphology evolution study, SEM measurements of hematite and reduced iron were conducted. The SEM images are presented in Fig. 8. The educt material is shown in Fig. 8a. The particle morphology is characterized by an aggregate structure composed of multiple primary particles, with the primary particle size on the order of 10^2 nm. The fully reduced iron particles, shown in Fig. 8 c), retain an aggregate structure, however, they exhibit secondary structures of similar size to the primary particles observed in the hematite sample. These aggregates form fractal-like configurations, appearing fragmented into even smaller primary particles with a size scale of approximately 10^1 nm. Since the particles at the intermediate stage could not be sampled directly, the reduction experiment has been repeated under the same conditions, and the particles were collected at a reduction degree of $\chi = 0.11$. The SEM image of a magnetite particle of this sample is shown in Fig. 8 b). It appears that the primary particles are less clearly distinguishable compared to the initial material. Domains with sizes comparable to the initial primary particles exhibit fine surface furrows, indicating that fragmentation into smaller structures has already commenced. An enlarged view of the reduced iron structure is provided in Fig. 9, demonstrating that the formation of the fractal structure aligns well with the results from the SAXS analysis. For full reduction, the additional scattering contribution observed in the SAXS curve is likely attributable to the formation of the fractal configuration, which exposes primary particles with size scales ranging from 10 up to 30 nm and beyond. Information on larger primary particles cannot be retrieved from the measured curves, due to the low resolution for lower scattering vectors. However, larger primary particles can also be detected by the SEM images.

5.4. Discussion

The observed morphological changes can be related to the iron nucleation during the reduction of the oxide. Before the formation to metallic iron, a slight restructuring of the surface already occurs through the formation of surface furrows during the magnetite formation. During the successive reduction to iron, metallic iron nucleates at the edges of the particles and subsequently grows further. As shown by the SEM images, the change of the scattering contribution between partial and full reduction is likely attributed to the growth of the nuclei at the edges of the reducing particles, which leads to the fractal structure observed in Fig. 8 c). Zhang et al. (2020b) summarizes the mechanisms driving morphology evolution during iron oxide reduction, emphasizing the interplay between reaction and diffusion rates. In a reaction-limited regime dominated by iron diffusion, fewer but larger nuclei form, which can grow into whisker-like structures. Conversely, in a diffusion-limited regime, supersaturation occurs, leading to the formation of a larger number of surface nuclei, which may result in porous structures. The reaction-limited regime typically prevails at high temperatures, while the diffusion-limited regime is commonly observed at lower temperatures. In the present work, the reduction occurred in a low-temperature, diffusion-limited regime. However, since the primary particles of hematite and the nuclei exhibit similar sizes, the resulting secondary structures appear more fragmented than porous.

6. Conclusion

In this work, an experimental method is proposed to investigate the morphology evolution of solid particles in a solid-gas heterogeneous reaction, using the reduction of iron oxide with hydrogen as an example. It was shown that lab-scale X-ray scattering techniques (SAXS/WAXS) can effectively measure the increase in specific surface area without removing the powder from the reactor. This was accomplished by embedding the particles in a boron nitride matrix within a capillary with optical access to enhance transmission. The proposed method enables the observation of iron nucleation and the growth of iron nuclei by detecting an increasing scattering contribution originating from formed nanostructures during the reduction process.

7. Additional material

7.1. Material properties of pure components

7.1.1. Mass specific total absorption coefficient and atomic scattering factors

7.1.2. Mass densities and isothermal compressibility of water

The mass density of pure water is evaluated by

$$\rho(T)/(\mathrm{g\,cm^{-3}}) = 10^{-3} \cdot \frac{a_0 + a_1 t + a_2 t^2 + a_3 t^3 + a_4 t^4 + a_5 t^5}{1 + a_6 t}, \tag{36}$$

where $a_0 = 999.83952$, $a_1 = 16.945176$, $a_2 = -7.9870401 \cdot 10^{-3}$, $a_3 = -46.170461 \cdot 10^{-6}$, $a_4 = 105.56302 \cdot 10^{-9}$, $a_5 = -280.54253 \cdot 10^{-12}$ and $a_6 = 16.878950 \cdot 10^{-3}$ and $t = T/°C$ (Kell, 1975). The compressibility of pure water is given by

$$\beta_T(T)/(\mathrm{Pa}) = 10^{-11} \cdot \frac{b_0 + b_1 t + b_2 t^2 + b_3 t^3 + b_4 t^4 + b_5 t^5}{1 + b_6 t}, \tag{37}$$

where $b_0 = 50.88496$, $b_1 = 0.6163813$, $b_2 = 1.459187 \cdot 10^{-3}$, $b_3 = 20.08438 \cdot 10^{-6}$, $b_4 = -58.47727 \cdot 10^{-9}$, $b_5 = 410.4110 \cdot 10^{-12}$ and $b_6 = 19.67348 \cdot 10^{-3}$ and $t = T/°C$ (Kell, 1975).

CRediT authorship contribution statement

Max Philipp Deutschmann: Writing – review & editing, Writing – original draft, Visualization, Methodology, Investigation, Formal analysis, Data curation, Conceptualization; **Hermann Nirschl:** Writing – review & editing, Writing – original draft, Supervision, Project administration, Funding acquisition.

Data availability

Data will be made available on request.

Declaration of Competing Interest

The authors declare that they have no known competing financial interests or personal relationships that could have appeared to influence the work reported in this paper.

Acknowledgments

This work was performed within the cluster project Clean Circles. Financial support from the Strategy Fund of the KIT Presidium and the Hessian Ministry of Higher Education, Research, Science and the Arts and the German Research Foundation (project no.: 558715615) is gratefully acknowledged. We thank K. Hirsch (Institute of Mechanical Process Engineering and Mechanics, Karlsruhe Institute of Technology) for his help with the measurements of the particle size distributions, as well as Dr. E. Müller (Laboratory for Electron Microscopy, Karlsruhe Institute of Technology) for his help with the scanning electron microscopy.

References

Bergthorson, J.M., 2018. Recyclable metal fuels for clean and compact zero-carbon power. Prog. Energy Combust. Sci. 68, 169–196. https://doi.org/10.1016/j.pecs.2018.05.001

Bouzakher-Ghomrasni, N., Taché, O., Leroy, J., Feltin, N., Testard, F., Chivas-Joly, C., 2021. Dimensional measurement of tio2 (nano) particles by SAXS and SEM in powder form. Talanta 234, 122619. https://doi.org/10.1016/j.talanta.2021.122619

Buchheiser, S., Deutschmann, M.P., Rhein, F., Allmang, A., Fedoryk, M., Stelzner, B., Harth, S., Trimis, D., Nirschl, H., 2023. Particle and phase analysis of combusted iron particles for energy storage and release. Materials 16 (5), 2009. https://doi.org/10.3390/ma16052009

Chavez Panduro, E.A., Beuvier, T., Fernández Martínez, M., Hassani, L., Calvignac, B., Boury, F., Gibaud, A., 2012. Small-angle X-ray scattering analysis of porous powders of $caCO_3$. J. Appl. Crystall. 45 (5), 881–889. https://doi.org/10.1107/S0021889812032219

Debiagi, P., Rocha, R.C., Scholtissek, A., Janicka, J., Hasse, C., 2022. Iron as a sustainable chemical carrier of renewable energy: analysis of opportunities and challenges for retrofitting coal-fired power plants. Renew. Sustain. Energy Rev. 165, 112579. https://doi.org/10.1016/j.rser.2022.112579

Dirven, L., Deen, N.G., Golombok, M., 2018. Dense energy carrier assessment of four combustible metal powders. Sustain. Energy Technol. Assessm. 30, 52–58. https://doi.org/10.1016/j.seta.2018.09.003

Glatter, O., Kratky, O. (Eds.), 1983. Small Angle X-ray Scattering. Academic Press, London; New York. 2. print edition.

Gong, X., Zhang, B., Wang, Z., Guo, Z., 2014. Insight of iron whisker sticking mechanism from iron atom diffusion and calculation of solid bridge radius. Metallurg. Mater. Trans. B 45 (6), 2050–2056. https://doi.org/10.1007/s11663-014-0125-9

Guo, L., Bao, Q., Gao, J., Zhu, Q., Guo, Z., 2020. A review on prevention of sticking during fluidized bed reduction of fine iron ore. ISIJ Int. 60 (1), 1–17. https://doi.org/10.2355/isijinternational.ISIJINT-2019-392

Halter, F., Jeanjean, S., Chauveau, C., Berro, Y., Balat-Pichelin, M., Brilhac, J.F., Andrieu, A., Schonnenbeck, C., Leyssens, G., Dumand, C., 2023. Recyclable metal fuels as future zero-carbon energy carrier. Appl. Energy Combust. Sci. 13, 100100. https://doi.org/10.1016/j.jaecs.2022.100100

Haynes, W.M., Lide, D.R., Bruno, T.J. (Eds.), 2017. CRC Handbook of Chemistry and Physics: A Ready-Reference Book of Chemical and Physical Data. CRC Press, Boca Raton, Florida. 2016–2017, 97th edition edition.

Hessels, C.J.M., Homan, T.A.M., Deen, N.G., Tang, Y., 2022. Reduction kinetics of combusted iron powder using hydrogen. Powder Technol. 407, 117540. https://doi.org/10.1016/j.powtec.2022.117540

Hessels, C.J.M., Smeets, A.H.J., Finotello, G., Deen, N.G., Tang, Y., 2023. Sintering behavior of combusted iron powder in a packed bed reactor with nitrogen and hydrogen. Particuology 83, 8–17. https://doi.org/10.1016/j.partic.2023.02.007

Julien, P., Bergthorson, J.M., 2017. Enabling the metal fuel economy: green recycling of metal fuels. Sustain. Energy Fuels 1 (3), 615–625. https://doi.org/10.1039/C7SE00004A

Kell, G.S., 1975. Density, thermal expansivity, and compressibility of liquid water from 0.deg. to 150.deg. correlations and tables for atmospheric pressure and saturation reviewed and expressed on 1968 temperature scale. J. Chem. Eng. Data 20 (1), 97–105. https://doi.org/10.1021/je60064a005

Komatina, M., Heinrich, W.G., 2004. The sticking problem during direct reduction of fine iron ore in the fluidized bed. Metalurgija-J. Metall. 10 (4), 309–328. https://doi.org/10.30544/378

Kuhn, C., Düll, A., Rohlfs, P., Tischer, S., Börnhorst, M., Deutschmann, O., 2022. Iron as recyclable energy carrier: feasibility study and kinetic analysis of iron oxide reduction. Appl. Energy Combust. Sci. 12, 100096. https://doi.org/10.1016/j.jaecs.2022.100096

Kuhn, C., Knapp, A., Deutschmann, M.P., Spielmann, J., Tischer, S., Kramm, U.I., Nirschl, H., Deutschmann, O., 2024. Iron as recyclable metal fuel: unraveling oxidation behavior and cyclization effects through thermogravimetric analysis, wide-angle x-ray scattering and mössbauer spectroscopy. Chem. Sus. Chem. 17 (15), e202400351. https://doi.org/10.1002/cssc.202400351

Li, J., Kong, J., Zhu, Q., Li, H., 2017. Efficient synthesis of iron nanoparticles by self-agglomeration in a fluidized bed. AIChE J. 63 (2), 459–468. https://doi.org/10.1002/aic.15402

Matsumura, G., 1971. Sintering of iron wires. Acta Metallur. 19 (8), 851–855. https://doi.org/10.1016/0001-6160(71)90141-6

Rambo, R.P., Tainer, J.A., 2011. Characterizing flexible and intrinsically unstructured biological macromolecules by SAS using the porod-debye law. Biopolymers 95 (8), 559–571. https://doi.org/10.1002/bip.21638

Schlumberger, C., Scherdel, C., Kriesten, M., Leicht, P., Keilbach, A., Ehmann, H., Kotnik, P., Reichenauer, G., Thommes, M., 2022. Reliable surface area determination of powders and meso/macroporous materials: small-angle X-ray scattering and gas physisorption. Micropor. Mesopor. Mater. 329, 111554. https://doi.org/10.1016/j.micromeso.2021.111554

Seltzer, S., 1995a. Tables of X-Ray Mass Attenuation Coefficients and Mass Energy-Absorption Coefficients, NIST Standard Reference Database 126. https://doi.org/10.18434/T4D01F

Seltzer, S., 1995b. X-ray Form Factor, Attenuation and Scattering Tables, NIST Standard Reference Database 66. https://doi.org/10.18434/T4HS32

Shkolnikov, E.I., Zhuk, A.Z., Vlaskin, M.S., 2011. Aluminum as energy carrier: feasibility analysis and current technologies overview. Renew. Sustain. Energy Rev. 15 (9), 4611–4623. https://doi.org/10.1016/j.rser.2011.07.091

Sohrabi, M., Ghobadian, B., Najafi, G., 2024. Toward a sustainable future: utilizing iron powder as a clean carrier in dry cycle applications. Int. J. Environ. Sci. Technol. . https://doi.org/10.1007/s13762-024-05529-4

Spalla, O., Lyonnard, S., Testard, F., 2003. Analysis of the small-angle intensity scattered by a porous and granular medium. J. Appl. Crystall. 36 (2), 338–347. https://doi.org/10.1107/S0021889803002279

Sperling, A., Deutschmann, M.P., Ning, D., Spielmann, J., Li, T., Kramm, U.I., Nirschl, H., Böhm, B., Dreizler, A., 2025. Oxidation progress and inner structure during single micron-sized iron particles combustion in a hot oxidizing atmosphere. Fuel 381, 133147. https://doi.org/10.1016/j.fuel.2024.133147

Zhang, X., He, S., Sun, H., Zhu, Q., Li, J., Li, H., 2020a. Mechanism of surface morphology evolution in the reduction of fine iron ore in a conical fluidized bed reactor. Chem. Eng. Sci. 220, 115468. https://doi.org/10.1016/j.ces.2019.115468

Zhang, X., He, S., Sun, H., Zhu, Q., Li, J., Li, H., 2020b. Mechanism of surface morphology evolution in the reduction of fine iron ore in a conical fluidized bed reactor. Chem. Eng. Sci. 220, 115468. https://doi.org/10.1016/j.ces.2019.115468